


Leading edge serrations for the reduction of aerofoil self-noise at low angle of attack, pre-stall and post-stall conditions

International Journal of Aeroacoustics
XX(X):2–34
© The Author(s) 2020
Reprints and permission:
sagepub.co.uk/journalsPermissions.nav
DOI: 10.1177/ToBeAssigned
www.sagepub.com/


Giovanni Lacagnina¹, Paruchuri Chaitanya², Jung-Hoon Kim²,
Tim Berk³, Phillip Joseph¹, Kwing-So Choi², Bharathram
Ganapathisubramani³, Seyed Mohammad Hasheminejad⁴, Tze
Pei Chong⁴, Oksana Stalnov⁵, Muhammad Farrukh Shahab⁶,
Mohammad Omidyeganeh⁶ and Alfredo Pinelli⁶

Abstract

This paper addresses the usefulness of leading edge serrations for reducing aerofoil self-noise over a wide range of angles of attack. Different serration geometries are studied over a range of Reynolds number ($Re \approx 2 \cdot 10^5 - 4 \cdot 10^5$). Design guidelines are proposed that permit noise reductions over most angles of attack. It is shown that serration geometries reduces the noise but adversely effect the aerodynamic performance suggesting that a trade-off should be sought between these two considerations. The self-noise performance of leading edge serrations has been shown to fall into three angle of attack (AoA) regimes: low angles where the flow is mostly attached, moderate angles where the flow is partially to fully separated, and high angles of attack where the flow is fully separated. Leading edge serrations have been demonstrated to be effective in reducing noise at low and high angles of attack but ineffective at moderate angles. The noise reduction mechanisms are explored in each of three angle regimes.

Keywords

Stall noise, Leading edge serrations, Noise reductions, Aerofoil Self-noise

Introduction

Leading edge serrations are well known to be able to enhance the aerodynamic performance of aerofoils (Fish (1994); Fish and Battle (1995); Fish et al. (2008)) and also in reducing their noise due to the interaction with turbulent in-flow (Roger et al. (2013); Lau and Kim (2013); Clair et al. (2013); Chaitanya et al. (2017)). Leading edge serrations are also shown to provide noise reductions in self-noise at relatively low angles of attack (Chaitanya et al. (2017)). In this paper we explore their potential for reducing aerofoil self-noise over a wide range of angles of attack, including pre-stall and post-stall conditions. Control of aerofoil self-noise at these range of attack angles and the reason behind it does not appear to have been addressed in previous literature.

The far-field self-noise generated by an aerofoil at low to moderate angle of attack is caused by the interaction between pressure fluctuations over the surface convecting past the trailing edge. At low AoA, where the flow remains attached over the entire surface, these hydrodynamic pressure fluctuations arise from the turbulent boundary layer in direct contact with the surface. At higher angles of attack, where the flow becomes separated from the trailing edge, the pressure fluctuations on the surface are the result of the near field from the turbulent shear layer.

A number of control techniques have been proposed aimed at reducing aerofoil noise at low AoA for which the flow is fully attached. Most of these methods involve introducing some kind of modification to the trailing edge, such as serrated edges (Hersh and Hayden (1971); Gruber et al. (2011); Moreau et al. (2011); Oerlemans et al. (2009)), porous surfaces (Geyer et al. (2010)) and brushes (Herr (2007); Finez et al.

¹Institute of Sound and Vibration Research, University of Southampton, UK

²Faculty of Engineering, University of Nottingham, UK

³Aerodynamics and Flight Mechanics Research Group, University of Southampton, UK

⁴Department of Mechanical, Aerospace and Civil Engineering, Brunel University, UK

⁵Technion—Israel Institute of Technology, Haifa, Israel

⁶School of Mathematics, Computer Science and Engineering, City University London, UK

Corresponding author:

Paruchuri Chaitanya, Institute of Sound and Vibration Research, University of Southampton, Southampton, SO17-1BJ, UK.
Email: ccp1m17@soton.ac.uk

(2010)). All these different methods have been tested experimentally in low Reynolds number flow conditions and have been shown able to deliver a noise reduction between 3 and 7 dB at low angles of attack.

All these noise control techniques have been conceived and tested on aerofoils at relatively low AoA. In many situations, however, the aerofoil is required to operate at higher AoA, for which partial separation has occurred. Examples of this include a wind turbine operating in high wind sheared flows and outlet guide vanes operating at off-design conditions. In these cases, trailing edge serrations are unlikely to be effective in reducing self-noise and alternative solutions must be sought.

Leading edge serrations have been widely investigated as a means of enhancing aerodynamic performance, particularly near stall conditions. They have the same effect on the flow as tubercles on Humpback Whale flippers [Fish \(1994\)](#), which are considered to act as lift-enhancement devices, capable of keeping the flow attached over a larger range of angles of attack thereby delaying stall ([Fish and Battle \(1995\)](#); [Fish et al. \(2008\)](#)) and increasing $C_{L_{max}}$ ([Miklosovic et al. \(2004\)](#)). The aerodynamic effect of tubercles wavelength and amplitude has been investigated, both for constant and varying values along the span ([Johari et al. \(2007\)](#); [Hansen et al. \(2011\)](#); [Sisinni et al. \(2013\)](#)).

The exact mechanism by which leading edge serrations on airfoils are able to delay stall is still not completely understood [Hansen et al. \(2016\)](#). A number of previous studies [Custodio \(2007\)](#); [Hansen et al. \(2009\)](#) on leading edge serrations have demonstrated the formation of streamwise vortices behind the serration tip. Due to the acceleration of the flow in the troughs between the serration peaks, a region of low pressure is established [Watts et al. \(2001\)](#). This low-pressure region leads to an entrainment of the flow behind the peaks and generate a pair of counter-rotating vortices downstream of each trough. It has been suggested by [Johari et al. \(2007\)](#); [Custodio \(2007\)](#); [Miklosovic et al. \(2007\)](#) that these vortices can induce a vortex lift or intensify the momentum exchange within the boundary layer and thus increase the flow attachment and postpone stall ([Fish and Battle \(1995\)](#); [Skillen et al. \(2014\)](#)). A number of researchers have suggested that leading-edge serrations are able to control stall via a mechanism similar to that of vortex generators which produce streamwise vortices that are typically on the scale of the boundary layer ([Miklosovic et al. \(2004\)](#); [Hansen et al. \(2011\)](#); [Zhang et al. \(2014\)](#)). however, there is no consensus on the precise control mechanism since the serration wavelength and amplitude are commonly much larger than the boundary layer thickness on the aerofoil. It has been proposed by [Van Nierop et al. \(2008\)](#) that the principal mechanism by which leading edge serrations are able to control stall is that they simply alter the pressure distribution on the aerofoil.

The purpose of this paper is to quantify and understand the balance between the effects on aerodynamic behaviour and noise obtained by the use of sinusoidal serrations introduced onto the aerofoil leading edge. The study will encompass a wide range of AoA, including pre-stall and post-stall conditions. The paper will investigate the sensitivity on aerodynamic and noise behaviour to variations in serration amplitude and wavelength. Detailed and simultaneous flow and acoustic measurements will be made to establish the noise reduction mechanism.

Aerofoil configurations and Experimental Setup

Aerofoil configurations

The effect of leading edge serrations on the noise and aerodynamics is investigated on a NACA65-(12)10 aerofoil, which is among a class of high-performance aerofoils, often used in cascades and turbines and designed to maximize the region of laminar flow over their surface (Abbott and Von Doenhoff (1959)). Two models were investigated, having chords of 0.1 m and 0.15 m and a common span of 0.35 m. Measurements were made at various flow speeds in the range of $U_\infty = 20 - 40$ m/s, corresponding to a Reynolds number in the range $[1.5 \cdot 10^5 - 4 \cdot 10^5]$. The serrations were designed to occupy the first 1/3 of the chord, keeping the rest of the aerofoil identical to the baseline aerofoil. The sinusoidal profile can be described by the wavelength λ and the amplitude h . Different combinations of h and λ investigated in this paper are summarized in table 1.

Name	Wavelength λ [mm]	Amplitude h [mm]	λ/h
L10H3	10	3	3.33
L10H6	10	6	1.67
L10H12	10	12	0.83
L20H3	20	3	6.67
L20H6	20	6	3.33
L20H12	20	12	1.67
L30H3	30	3	10
L30H6	30	6	5
L30H12	30	12	2.5

Table 1. Characteristics of the different serration geometries

The chord length c at any radial position r along the aerofoil is of the form $c(r) = c_0 + h \sin(2\pi r/\lambda)$, where c_0 is the baseline chord length, thus ensuring that the wetted area remains constant between serrated and unserrated aerofoils. The aerofoil

profile $y(X, r)$ at any position r along the aerofoil can be described in terms of function g as

$$y(X, r) = \begin{cases} g(x/c_0), & 0 < x/c_0 < 2/3 \\ g(x/c(r)), & 2/3 < x/c(r) < 1 \end{cases} \quad (1)$$

where $X = 0$ is the trailing edge, $X = 1$ is the leading edge and r is the spanwise coordinate, as shown in figure 1.

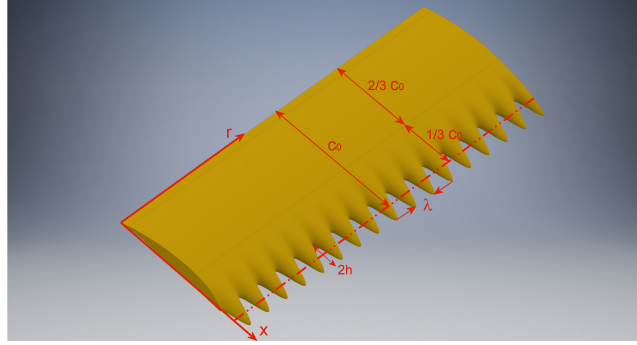


Figure 1. A sketch of the LE serrated aerofoil displaying its geometrical parameters

Experimental Facility

Most of noise and flow measurements were performed in the open jet wind tunnel facility at the Institute of Sound and Vibration Research (ISVR), at the University of Southampton. Photographs of the facility and the experimental set up are shown in figure 2. A detailed description of the wind tunnel can be found in [Chong et al. \(2009\)](#). It is enclosed inside the university's large anechoic chamber, sized 8 m x 8 m x 8 m, whose walls are acoustically treated with glass wool wedges to get a cut-off frequencies of 80 Hz. The nozzle dimensions are 0.5 m in height and 0.35 m in width. This height of nozzle together with the chord length of 0.1 - 0.15 m, ensures that the downwash deflection of the jet is sufficiently small to allow measurements near stall conditions. The ratio between the geometrical angle of attack α_{geom} and the effective angle α_{eff} , i.e. after flow deflection has been taken into account, can be estimated from the relationship derived by [Brooks et al. \(1984\)](#), which applied to the current configuration, for $c_0=0.1$ m and $c=0.15$ m respectively, is:

$$\zeta = \frac{\alpha_{geom}}{\alpha_{eff}} \approx 1.3 - 1.5 \quad (2)$$

where $\zeta = (1 + 2\sigma)^2 + \sqrt{12\sigma}$, $\sigma = (\frac{\pi^2 c_0}{48 H})^2$, and H the nozzle height. Two side plates attached to the side walls of the nozzle maintain the two-dimensionality of the flow and hold in place the aerofoil such that the leading edge of the aerofoil is one chord-length downstream of the nozzle lip. **Please note the above Eq. (2) is only valid to acoustic measurements as they are performed on open jet wind tunnel facility.**

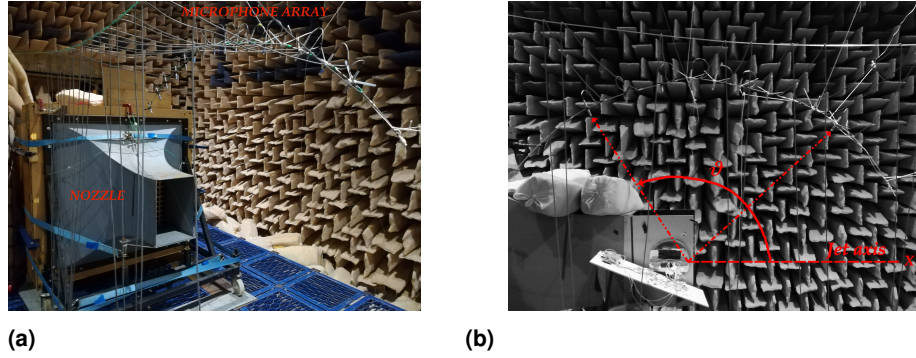


Figure 2. a) Open wind tunnel and acoustic setup inside the ISVR's anechoic chamber; b) Microphones emission angles

Aerodynamic force measurements were carried out in an closed open-return wind tunnel at the University of Nottingham. The dimension of the test section is 0.91 m wide x 0.75 m high and 1.5 m long. In these tests, a vertically installed aerofoil model was positioned at the mid-span, 0.1 m above the floor and 0.7 m downstream from the inlet of the test section. A schematic and more details of the experimental set-up is shown in Jung-Hoon KIM et al. (2019). The aerofoil was connected to a force balance by an aluminium strut which was covered by an aerodynamic shaped fairing fixed to the wind tunnel floor. A circular plate in 150 mm diameter was attached to the bottom of the aerofoil, which was set in a circular hole provided by a 360 mm x 260 mm rectangular endplate. This allows the aerofoil to rotate through its transverse axis to change the angle of attack during the measurements. A 3-component force transducer (Kyowa, LSM-B-SA1, rated capacity: 10 N) was used to measure the drag and the lift on the aerofoil. The force balance was mounted on a turntable which was connected through a 2:1 gear to a stepping motor. As the aerodynamic measurements are performed on closed circuit wind tunnel, the effective AoA, α_{eff} is same as geometric AoA, α_{geo} .

Measurement Procedure

Acoustic pressure measurements were made using a polar array of ten half-inch condenser microphones (B&K type 4189), located at the mid span plane of the aerofoil at a distance of 1.2 m from its trailing edge, as shown in figure 2. The microphone emission angles range from 40 to 130°, relative to the aerofoil trailing edge and downstream direction of the jet axis. Measurements were performed at a sampling frequency of 40 kHz for a duration of 20 s.

Steady and Unsteady pressure on aerofoil surface

The surface pressure spectra over the aerofoil surface were estimated with remote microphone method, with a number of capillary tubes that run below the aerofoil surface between pressure taps, along the aerofoil chord and along the span close to the trailing edge, and a number of T-junctions connected to miniature microphones. The microphones are 2.5 mm diameter omni-directional electret condenser microphones (Knowles Electronics 206 FG-3329-P07). On the opposite side of the T-junction are additional capillary tubes, approximately 3 m in length, to avoid reflections from the closed end. Surface pressure measurements were likewise acquired for a duration of 20 s at a sampling frequency of 40 kHz. Special care was given to the sealing of the microphone within the T-junction block, which was found to affect the pressure measurements. The miniature microphones were calibrated in-situ against a reference $\frac{1}{4}$ inch condenser microphone by means of an in-duct loudspeaker. [More details about the surface pressure measurement setup were discussed in Stalnov et al. \(2016\).](#)

PIV measurement

The velocity field around the aerofoil was investigated by means of the Time Resolved Particle Image Velocimetry (TRPIV) setup shown in the photograph in Figure 3. Velocity data was obtained at a frequency of 4 kHz and based on the acquisition of roughly 20,000 images, corresponding to 5 s of data. A Nd:YLF laser capable of a high-repetition rate of up to 10 kHz was used to generate a light beam, then converted by a system of cylindrical and spherical lenses into a light sheet of 1 mm thickness with which to illuminate the vertical plane along the chord of the aerofoil in the streamwise direction. Two high speed Phantom v641 cameras, set at a resolution of 1024 x 512 pixels (0.5 MP) and in a T-shape configuration, were used to frame the area around the aerofoil, primarily on the suction side, as shown in figure 3 (Right). The cameras have a 10 μm sensor pixel size and are equipped with an 85 mm focal length lens. The flow was seeded using a Martin Magnum 1200 smoke machine, positioned at

the inlet of the centrifugal fan of the wind tunnel, which provided a uniform particle distribution of the flow from the nozzle with diameters of roughly $1 \mu\text{m}$. From the raw images, the average particle image size was assessed to be approximately 2.2 pixels and the number of particles per pixel (N_{ppp}) was about 0.038. This value is close to the optimal value prescribed by Willert and Gharib of ($N_{ppp} = 0.035$) Willert and Gharib (1991) and in agreement with the recommendations of Raffel et al. (2007) and Cierpka et al. (2013) ($0.03 < N_{ppp} < 0.05$). Lastly, the magnification factor M was about 6.7 pixel/mm (roughly 0.15 mm/pixel).

The PIV images were processed using digital cross-correlation analysis (Willert and Gharib (1991)). A multi-grid/multi-pass algorithm (Soria (1996)), with an iterative image deformation (Scarano (2001); Huang et al. (1993); Jambunathan et al. (1995); Nogueira et al. (1999)) was applied to compute the instantaneous velocity fields, setting the final interrogation window size as 32×32 pixels with an overlap factor of 75%. Spurious vectors are eliminated by means of a vector validation algorithm, based on a regional median filter (Westerweel and Scarano (2005)), with a kernel region of 3×3 vectors, and group removing.

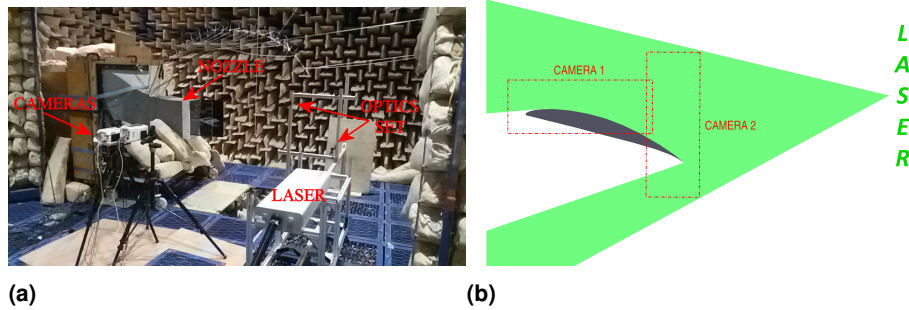


Figure 3. a) TRPIV setup inside the ISVR's anechoic chamber; b) Sketch showing the PIV cameras fields-of-view (dashed lines) and the total framed area.

Results

Aerodynamic characteristics of baseline aerofoil

Most of the aerodynamic and aeroacoustic measurements presented in this paper were performed with an aerofoil 0.1 m chord. Before investigating the aerofoil noise characteristic over the range of angles of attack, including pre-stall and post-stall conditions, we first consider the variation in the C_p distribution and lift and drag over this range of angles. The main purpose of this measurement is to quantify the

development of the separated flow region with increasing AoA. The aerodynamic measurements were made in the closed wind tunnel at the University of Nottingham at a free-stream velocity of $U_\infty = 15 \text{ m/s}$. Figure 4 shows the variation in C_p at the angles of attack of 0° , 4° , 7° , 11° , 13° , 18° and 20° .

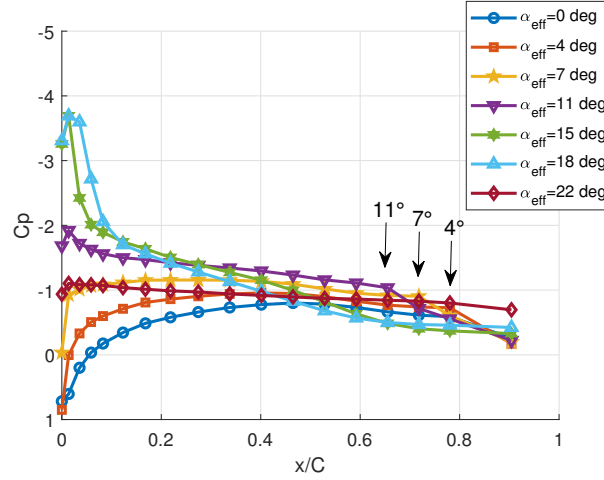


Figure 4. Pressure distribution on the NACA65(12)10 aerofoil suction side at different angles of attack. $U_\infty = 15 \text{ m/s}$;

Fig 4 provides clear evidence of separation even at very low angles of attack. At $\alpha = 4^\circ$, separation is observed to occur at about 20% of the chord from the trailing edge, which then moves upstream to 28% and 35% at the AoA of 7° and 11° respectively. Between the AoA of 11° and 15° , the location of separation moves much closer to the leading edge reaching a maximum distance of about 90% from the trailing edge. At the highest AoA under consideration of 22° , the aerofoil is fully stalled and the C_p distribution is relatively flat.

A comparison of the overall lift and drag coefficient variation with AoA is shown in Figs 5. The lift coefficient variation can be observed to increase at a constant slope until about 11° when it begins to gradually fall, which is characteristic of a *trailing edge stall* (Anderson Jr (2010)), and further peaking again at about 16° . Above this angle the lift coefficient falls significantly. This angle will be shown below to correspond to an important angle which delineates the transition between negligible noise reductions and modest noise reductions of up to $\sim 2\text{dB}$. The drag coefficient increases relatively slowly below about 16° but then increases at a faster rate at angles above this.

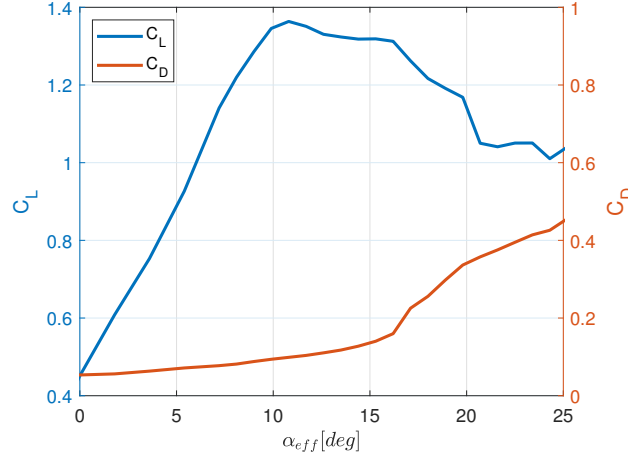


Figure 5. Lift and drag curves versus angle of attack

Noise characteristics due to baseline aerofoil

Before presenting the measured noise reductions due to leading edge serrations we first investigate the noise characteristics of the untreated baseline airfoil. Aerofoil noise at high angles of attack has been measured in a number of previous studies (Brooks et al. (1989); Moreau et al. (2009); Schuele and Rossignol (2013); Suryadi and Herr (2015); Bertagnolio et al. (2017)). The noise spectrum associated with flow separation is characterized by a spectral hump centred at relatively low frequencies determined by the dimensions of the separated zone, such as the boundary layer thickness (Brooks et al. (1989)) or the distance from the trailing edge at which separation occurs (Bertagnolio et al. (2017)). We conclude from these findings that the noise spectrum is predominantly determined by the eddy structures within the separated flow.

Figure 6 is a colour map showing the variation in sound power level versus frequency and effective angle of attack (obtained from the correction of Eq. (1)), relative to the noise at 0° . Sound Power Level spectra $PWL(f)$ are calculated by integrating the pressure spectra over the polar array of 16 microphones using the procedure described in Narayanan et al. (2015). This figure comprises of noise data obtained at 12 angles of attack between $AoA = 0.0^\circ$ and 22° , which have been interpolated for ease of visualization.

The bandwidth of the spectral hump characteristic of separation noise can be observed to increase while its centre frequency decreases with increasing AoA. Particularly striking is the sharp increase in noise at 11° which coincides with the

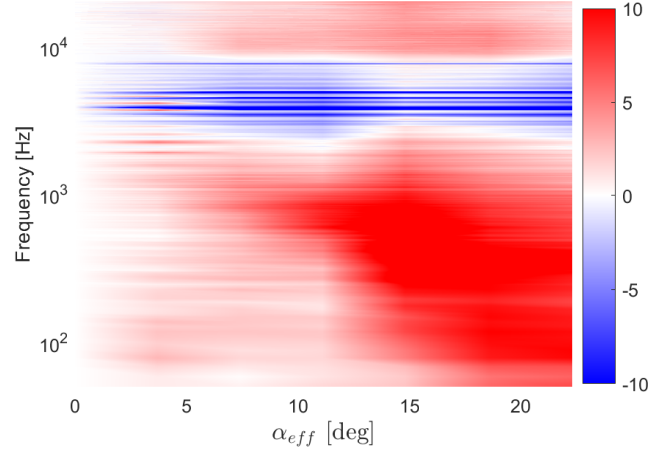


Figure 6. Change in sound power level ($PWL_{AoA} - PWL_{AoA=0}$) with the angle of attack compared to $\alpha_{eff} = 0^\circ$ for the NACA65(12)10 aerofoil at $U_\infty = 40$ m/s

first peak in the C_L curve in Figure 5. Note that no apparent increase in noise at 16° is observed at which the aerofoil is fully stalled and there is a significant drop in lift. However, we will show below that this angle is important in determining the effectiveness of leading edge serrations on noise reductions.

The behaviour of the noise spectra with AoA is more clearly seen in Figure 7, which shows the Sound Power Level spectra compared at seven angles of attack between 0° and 22° . The spectral humps are now more clearly seen whose peak frequencies shift towards lower frequencies as the AoA is increased from 0° to 15° . At the higher AoA of 19° and 22° no spectral hump can be observed and the spectra decay smoothly with frequency as the airfoil is fully stalled. Also shown, as circles, are the centre frequencies f_{x_0} of the spectral hump calculated from the assumption that f_{x_0} occurs at a constant Strouhal number St_{x_0} defined with respect to the distance x_0 from the trailing edge at which separation occurs (Bertagnolio et al. (2017)). This centre frequency is therefore given by,

$$f_{x_0} = \frac{St_{x_0} U}{x_0} \quad (3)$$

where $St_{x_0} = 0.9$ is the value which provides best agreement with the measured centre frequencies. Here, x_0 is estimated from the C_p curves plotted in Figure 4. Very close agreement of within 100Hz can be observed between the predicted and measured centre frequencies suggesting that the coherent structures responsible for the spectral

hump occur in the region of separation of length x_0 . This is also consistent with the model due to Brooks et al. (1989), who predicts the peak frequency based on Strouhal number defined with respect to the boundary layer thickness, or rather the extension of the flow separated region (Lacagnina et al. (2019)). Please note the high frequency tones observed at low angles of attack is due to laminar boundary layer instabilities as the aerofoil is not tripped.

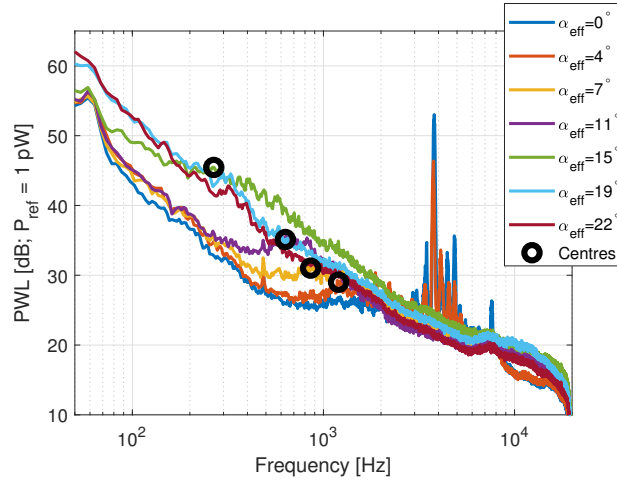


Figure 7. Noise results for the baseline NACA65(12)10 aerofoil at $U_\infty = 40$ m/s: Sound Power Level $PWL(f)$ at different angles of attack.

Noise characteristics due to serrated aerofoils

In this section we present the noise reductions for the serration geometries introduced in Table 1, comprising all combinations of the three serration amplitudes of 3, 6 and 12 mm ($h/c = 0.03, 0.06, 0.12$) and three wavelengths of 10, 20 and 30 mm ($\lambda/c = 0.1, 0.2$ and 0.3). The noise measurements were made at a flow speed of 40 m/s at seven effective AoA between 0° and 22° . The overall noise reductions in the frequency range between 100 Hz and 1 kHz for which separation noise is dominant are plotted in figure 8a and b for the three serrations of smallest wavelength of 10 mm and six serrations of larger wavelengths of 20 and 30 mm respectively. Also overlaid on this plot is the corresponding measurement of lift versus AoA for the baseline aerofoil.

The variation in overall noise reductions versus AoA can be observed to fall into three angle regimes I, II and III corresponding approximately to $AoA \lesssim 8^\circ$, $8^\circ \lesssim AoA \lesssim 16^\circ$, $AoA \gtrsim 16^\circ$, respectively. Levels of overall noise reduction of up to 3dB can be

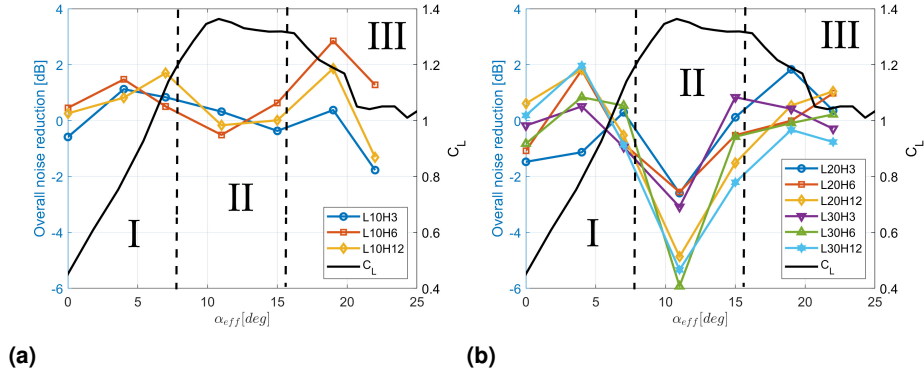


Figure 8. Trend of the reduction of separation noise ($f \approx 10^2 - 10^3$) for different leading edge serration geometries and different angles of attack; a) Small wavelength; b) Large wavelength

observed at low and high AoA (I and III), with the level of performance appearing to be sensitive to the serration amplitude, particularly at high AoA. In angle regime I ($< 8^\circ$) a small noise reduction is observed, peaking at about 1.5 dB. In angle regime III ($> 16^\circ$) at which full stall occurs, noise reductions are significantly greater for the best performing serration amplitude. However, in angle regime II ($8^\circ < \text{AoA} < 16^\circ$), noise reductions are relatively poor being consistently less than 0.5 dB. Note that these limiting values of angle of attack for each angle regime are approximate due to the limited number of angles of attack investigated.

To understand the noise reduction mechanisms in the three angle regimes, we investigate the noise reduction spectra for a representative angle in each regime. Figure 9a - c below shows a comparison of the Sound Power Level spectra for the baseline aerofoil and the L10H12 serration at the three representative AoA of 7° , 11° and 19° respectively. This serration was selected as a representative example whose performance is similar to that of the L10H6 and L10H3 serrations of the same wavelength, investigated previously .

From hereon all noise reduction spectra will plotted against non-dimensional frequency $St_c = \frac{f c}{U}$ to generalize the results. Figure 9a shows noise reduction at $\text{AoA} = 7^\circ$ of between 2 and 3 dB at frequencies below and above the frequencies of the spectrum hump ($1 < St_c < 4$), characteristic of separation noise discussed above. At this AoA the centre frequency f_{x_0} remains mostly unchanged by the introduction of the serration suggesting that the location of the separation remains unchanged. This observation is consistent with the limited change in lift, plotted in Figure 11, resulting from the introduction of the serration. The broadband reduction in noise therefore

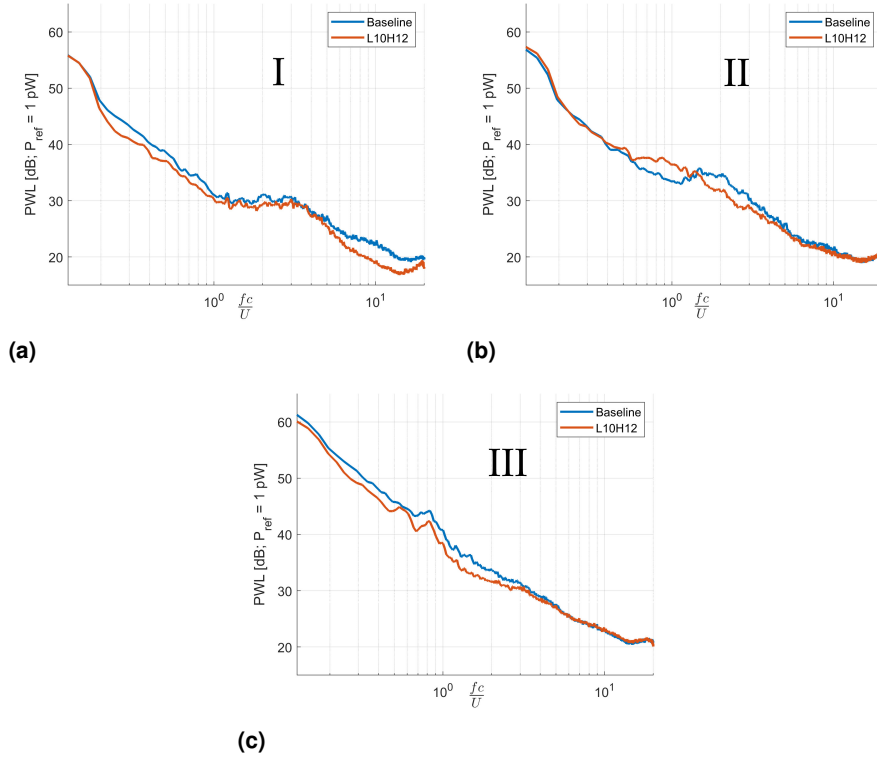


Figure 9. Far-field noise emitted spectra of the baseline and serrated aerofoils (L10H12) at different angles of attack: a) $\alpha_{eff} = 7^\circ$ (low AoA); b) $\alpha_{eff} = 11^\circ$ (mid AoA); c) $\alpha_{eff} = 19^\circ$ (high AoA);

could occur through a reduction in the shear layer turbulence as it convects past the trailing edge. This hypothesis will be investigated in more detail in section reduction mechanisms below.

At $AoA = 11^\circ$, which is in the range of angles for which there is negligible reduction in overall noise (angle regime II), the comparison of the Sound Power Spectra plotted in Figure 9b shows a clear shift in the spectral hump centre frequency from $St_c \approx 2$ to $St_c \approx 0.8$ between the baseline and serrated geometry. This shift strongly indicates that separation now occurs closer to the leading edge as a consequence of the leading edge serration. At this AoA, at which the baseline aerofoil provides maximum lift, the lift is most adversely affected by the introduction of the serration. Finally, at $AoA = 19^\circ$ where full stall occurs (angle regime III), the shape of the Sound Power Spectra remain similar with and without serration, but with typical noise reductions of up to 3 dB at frequencies below $St_c = 4$. In the angle regime the lift of the serrated aerofoil is

comparable with that of the baseline aerofoil but slightly exceeds it for the highest AoA. We will show in section below that noise reductions in this post-stall regime occur by shifting the shear layer further away from the trailing edge.

Figure 8a has demonstrated that, for the leading edge serration with the smallest wavelength under consideration, it is possible to obtain noise reductions over a wide range of angles of attack. We now consider the effect on the noise reductions of increasing the serration wavelength. Figure 8b shows the variation in overall noise reduction in the frequency range between 100 Hz and 1000 Hz versus AoA for six different serration profiles comprising all combinations of two wavelengths of 20 mm and 30 mm and three serration amplitudes of 3 mm, 6 mm and 12 mm. Again we overlay the variation in lift of the baseline aerofoil for comparison.

A similar trend with AoA can be observed for these six cases as was observed for the smallest wavelength plotted in Figure 8a, with the general behaviour being grouped into three angle regimes. In general, noise reductions are obtained at low AoA for which the flow is partially attached, and at high AoA for which full separation occurs. However, relatively large increases in noise are now observed in the range of AoA in between.

Finally, to understand in greater detail the dependence of noise reductions due to serration geometry, the noise reduction data plotted in Figure 8a and b are shown again in Figure 10a and b now plotted against the ratio λ/h for the AoA regimes I and III. Also shown in this figure is the corresponding maximum lift coefficient. **Please note in figure 10 for each geometry we use the maximum noise increase or reduction that are achieved for small angles ($\alpha_{eff} \leq 8^\circ$) and then the maximum noise increase or reduction for high angles ($16^\circ \lesssim \alpha_{eff} \gtrsim 22^\circ$).**

The noise reductions in Figure 10a show a clear trend with λ/h . Overall noise reductions in this range of low AoA can be observed to improve as λ/h is reduced. This figure identifies a critical value of λ/h of approximately 5, above which there is an overall noise increase. The corresponding variation in lift coefficient with λ/h can be observed to follow the opposite trend to the noise variation, where a variation in maximum lift of up to 20% can be observed. Thus, the leading edge serration geometry should be chosen that achieves a balance between aerodynamic and noise considerations. However, the precise reason for this critical value observed at low angles of attack regime is currently unknown.

By contrast, no clear trend is evident in Fig 10b for the variation in the noise reductions versus λ/h for the higher AoA conditions. More work is required to understand the variation in the noise reduction due to serration wavelength at higher AoA conditions.

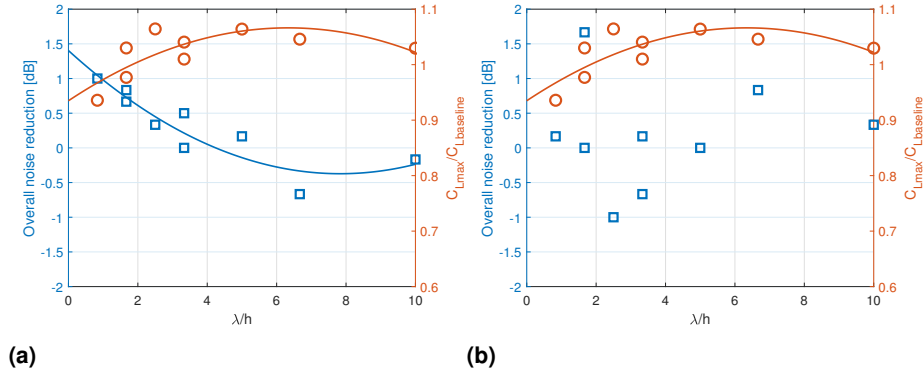


Figure 10. Average noise reduction in the frequency range ($10^2 - 10^3$) Hz as a function of serration geometry (sweep angle λ/h) a) Low angles of attack ($\alpha_{eff} \leq 8^\circ$); b) High angles of attack ($16^\circ \lesssim \alpha_{eff} \lesssim 22^\circ$)

Serrated Aerofoil Lift

An important requirement for design modification to an aerofoil geometry is that its aerodynamic performance is not too adversely affected. The lift generated by the baseline aerofoil and the two serration geometries L10H12 and L30H6 were measured by means of a 3-component force transducer (Kyowa, LSM-B-10NSA1, 10 N). The lift versus AoA is shown in figure 11.

The L30H6 serration with the largest wavelength can be observed to provide improved lift performance over all AoA compared to the baseline aerofoil. Less improved performance can be observed for the serration with the smaller wavelength, except near stall where the lift is lower. This behaviour is opposite to the behaviour observed for the noise reductions shown in figure 8 providing further confirmation that aerodynamic and acoustic behaviour exhibit opposite trends.

Reduction mechanisms

This section is concerned with the understanding of the noise reduction mechanisms associated with leading edge serrations for each of the three angle regimes identified above. We now consider each of these in turn.

Angle regime I: Low angles of attack ($AoA \lesssim 8^\circ$); partial separation

For the three angles of attack lying in angle regime I indicated in figure 8, clear overall noise reductions can be observed. In order to understand the mechanism associated

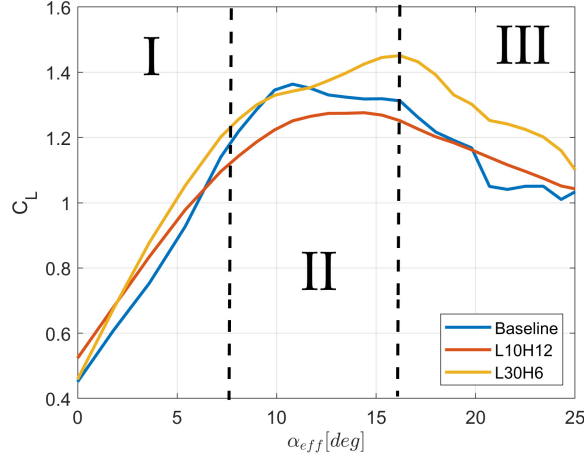


Figure 11. Lift coefficient for the baseline and two different serrated aerofoils (L10H12; L30H6)

with this reduction we first investigate the flow field around the aerofoil by means of a planar PIV measurement for a baseline aerofoil and the L30H6 serrated aerofoil. This serration was previously shown to provide greater lift over all AoA compared to the baseline aerofoil (see figure 11) as well as providing overall noise reductions of approximately 1dB at AoA below about 8° (see figure 8)

Figures 12a, c and e on the left hand side of this figure show the RMS value of the streamwise velocity component (u') while the right hand side 12b, d and f show the vertical (v') component in the vicinity of the aerofoil trailing edge. Results are shown over a vertical plane for the baseline case, over a plane aligned with the serration root and also a plane aligned with the serration peak. The effective AoA was $\alpha_{eff} = 7^\circ$ and the free-stream velocity was $U_\infty = 20 \text{ m/s}$, corresponding to the maximum velocity that could be tested due to limitations with the PIV set up. Note that the Reynolds number for this PIV measurement is half that of the noise measurement. However, the PIV results are used only as a means of providing a qualitative understanding of the noise reduction mechanisms. Furthermore, Reynolds number effects are not anticipated to be significant in this low Reynolds number regime below $5 \cdot 10^5$ where transition to turbulence starts to occur (Brendel and Mueller (1988)).

Introducing serrations at the leading edge can be observed to have a clear effect on the boundary layer near the trailing edge where reductions in turbulent RMS velocity of about 50% can be observed in both root and tip planes for both velocity components. Improved spectral information on the turbulence velocity near the trailing edge was

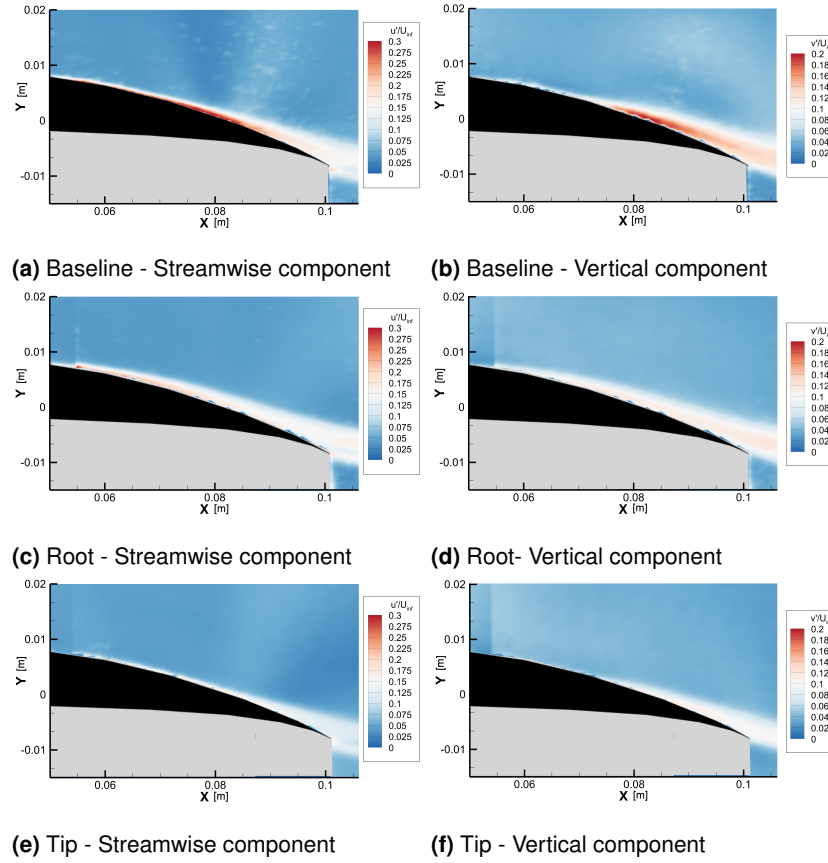


Figure 12. Contour plot of the two components of the velocity fluctuations as measured around the downstream part of the aerofoil at $\alpha_{eff} = 7^\circ$ (low AoA) and $U_\infty = 20 \text{ m/s}$. Streamwise velocity component (Left); Vertical velocity component (Right). The cases are: a,b) Baseline configuration; c,d) Plane crossing the root of the LE serrated configuration; e,f) Plane crossing the tip of the LE serrated configuration.

obtained using Hot Wire anemometry. This velocity information will be used in the next section as input data to the TNO model to assess whether the reduction in far field noise is consistent with the modification to the boundary layer caused by the introduction of leading edge serrations. A single hot wire was traversed vertically 1 mm downstream of the trailing edge, 5 cm above and below the trailing edge in 50 equal intervals. This range of heights above and below the trailing edge provides a good representation of the boundary layer close to the trailing edge on both pressure and suction sides for both baseline and serrated L30H6 aerofoils. Here, the measurements were performed near the root of the serration, since this was the location where the

minimum reduction of fluctuations compared to baseline aerofoil are observed, or in other words the maximum level of fluctuating velocities for the serrated aerofoil. It is also known from previous studies that the root is the dominant source of noise due to enhanced streamwise vortices. Chaitanya et al. (2017). Velocity data was acquired for 10 s at a 20 kHz sampling frequency at $U_\infty = 40 \text{ m/s}$.

The velocity spectra measured closest to the trailing edge for the baseline and serrated aerofoils is shown in Figure 13. The leading edge serration can be observed to provide substantial reductions in the mean square velocity by about 10dB at frequencies fc/U below about 4. Above this frequency, the spectra begin to converge and the reduction falls to about 2dB. Clearly, therefore, leading edge serrations have greatest influence on the boundary layer at low frequencies, This behaviour is broadly consistent with the difference in noise reduction spectra plotted in Figure 9a, with the exception being in the frequency range $1 < fc/U < 4$, which we have shown in Eq. (3) is related to the size of the separation bubble, which cannot be detected in the wake turbulence.

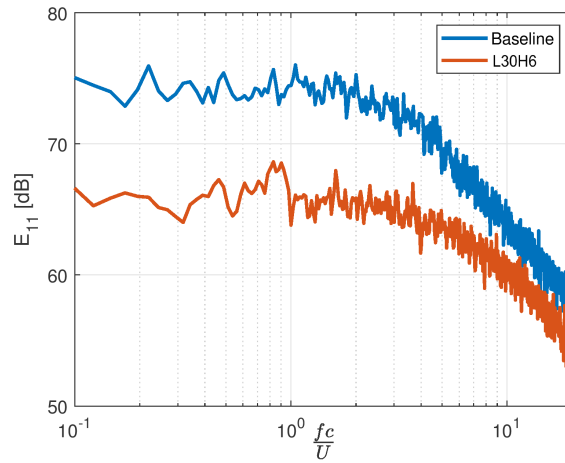


Figure 13. Power spectral densities of the axial velocity component E_{11} for baseline and serrated aerofoils at $\alpha_{eff} \approx 11^\circ$

TNO model

PIV velocity data shown in Figure 12 has clearly demonstrated that leading edge serrations can reduce the turbulence in the boundary layer close to the trailing edge at low to moderate AoA. In this section the hot wire velocity data is input into the classical TNO model for predicting the surface pressure spectrum beneath the boundary layer (Blake (1986); Parchen (1998)). The aim of this investigation is to assess whether the modification to the turbulent boundary layer is consistent with the reduction in

far field noise. The classical theory due to [Amiet \(1976\)](#) has demonstrated a direct relationship between the far-field radiated power spectral density of acoustic pressure $S_{pp}(x_1, x_2, x_3 = 0, \omega)$ to the near-field wall pressure wavenumber-frequency spectral density $S_{qq}(k_1, k_3, \omega)$ evaluated close to the trailing edge. Here x_1 , x_2 and x_3 are the streamwise, vertical and spanwise direction axes.

The surface pressure wavenumber - frequency spectrum $S_{qq}(k_1, k_3, \omega)$ can be predicted using the TNO model, which is based on the [Kraichnan \(1956\)](#) solution to the Poisson equation, together with simplifications proposed by [Blake \(1986\)](#) and [Parchen \(1998\)](#), and is of the form,

$$S_{qq}(k_1, k_3, \omega) = 4\rho_0^2 \frac{k_1^2}{k^2} \int_0^{\delta_{BL}} \Lambda_{2|22}(x_2) \left(\frac{\partial U_1}{\partial x_2} \right)^2 \overline{u_2^2}(x_2) \phi_{22}(k_1, k_3) \cdot \Phi_m(\omega - U_c(x_2)k_1) e^{-2|k|x_2} dx_2 \quad (4)$$

In this expression ρ_0 is the fluid density, δ_{BL} is the boundary layer thickness and $U_c(x_2)$ is the effective convection speed of the boundary layer eddies over the aerofoil surface at height x_2 above the surface. A wide range of methods have been proposed to evaluate this quantity. One of the most widely used is the spectral approach proposed by [Romano \(1995\)](#). The terms $\Lambda_{2|22}(x_2)$ is the velocity integral scale in wall normal direction, $\frac{\partial U_1}{\partial x_2}$ is the mean shear rate, $\overline{u_2^2}$ is the mean square of the velocity fluctuations in the vertical direction, ϕ_{22} is the dimensionless wavenumber spectral density of the vertically directed velocity fluctuations, and Φ_m is the moving axis spectrum that describes how the $\phi_{22}(k_1, k_3)$ spectrum of the vertical velocity fluctuations is distorted as a result of the generation and distortion of the eddies during convection over the trailing edge at a convection speed $U_c(x_2)$, all evaluated at height x_2 above the surface. More details about this approach is described in [Stalnov et al. \(2016\)](#).

The Hot Wire velocity data was used to compute the boundary layer thickness δ_{BL} , the mean shear rate $\frac{\partial U_1}{\partial x_2}$ and mean square velocity $\overline{u_2^2}(x_2)$, while the length-scale $\Lambda_{2|22}(x_2)$ and the velocity spectra ϕ_{22} were estimated using the semi-empirical relationships summarised by [Stalnov et al. \(2016\)](#). We make the assumption of "frozen turbulence", and hence

$$\Phi_m(\omega - U_c(x_2)k_1) = \delta(\omega - U_c(x_2)k_1) \quad (5)$$

such that only the wavenumber $k_1 = \omega/U_c(x_2)$ contributes to the integral at height x_2 . Finally, we assume that the observer is in the mid-span plane and hence only $k_3 = 0$ is of interest [Amiet \(1976\)](#).

Predictions of the difference in surface pressure spectra $S_{qq}(k_1, k_3 = 0, \omega)$ in dB between the baseline and serrated aerofoils are compared in figure 14 against the difference in far field noise power level in dB, plotted in Figure 9. **Note that the predicted difference includes contributions from both the suction and pressure sides. However, the contribution from the pressure side is smaller than compare to suction side due to thinner boundary layer.**

Good qualitative agreement between the difference in predicted and measured spectra can be observed suggesting that the reduction in far field noise resulting from the introductions of leading edge serration is consistent with the modification to the turbulent boundary layer.

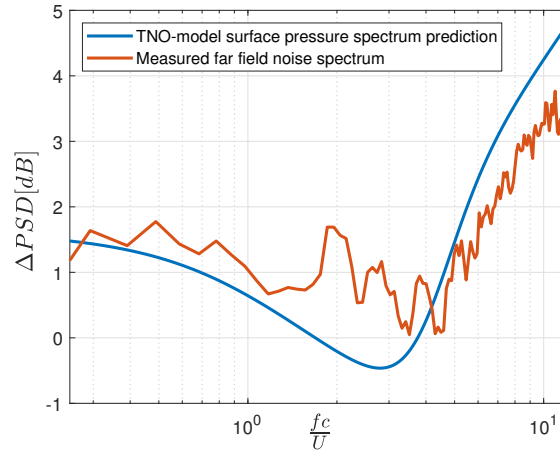


Figure 14. Comparison between the predicted reduction in surface pressure spectrum by TNO model and the measured reduction of far field noise spectrum.

Simultaneous surface pressure and far field noise

Finally, to gain further insight into the noise reduction mechanism at this low angle of attack the coherence spectrum was measured between a pressure sensor located 5mm from the suction side trailing edge and a far field microphone located 1.2m directly above the trailing at mid-span. In order to locate the pressure probes close to the trailing edge a larger aerofoil was used of 0.15m chord. Note that in this study we are only concerned with providing a qualitative understanding of the noise reduction mechanism. The coherence spectrum is plotted in Figure 15 against non-dimensional frequency fc/U . High coherence levels are indicative of coherent structures that radiate strongly to the far field and establish a causal relationship between a point in the far field and a single point on the trailing edge.

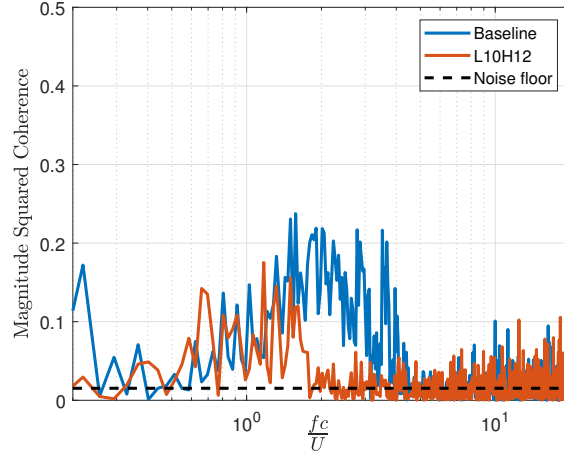


Figure 15. Coherence between noise and surface pressure at TE for baseline and serrated aerofoils at $\alpha_{eff} \approx 7^\circ$

This figure can be directly compared to Figure 9a for the baseline and serrated aerofoil noise spectra. The coherence is negligible for both baseline and serrated aerofoils at low frequencies ($fc/U < 1$) and high frequencies ($fc/U > 4$), where noise reductions are greatest. This observation is consistent with the noise reductions being due to a reduction in turbulence, as shown in figure 12, and not to modifications to the separation region, which we shall show below is important in the noise generation mechanism at higher angles of attack. The small peak in the coherence spectrum due to the baseline aerofoil can be seen to be reduced in level and frequency by the leading edge serration, suggesting that the leading edge serration has had a small effect on suppressing separation at this relatively small AoA, although the effect on noise in this frequency band is negligible (figure 9a).

Leading edge serrations are therefore an effective means of reducing boundary layer turbulence at small to moderate AoA, however, the mechanism by which this occurs is currently not well understood.

Angle regime II. Mid angles of attack ($8^\circ \lesssim AoA \lesssim 16^\circ$), partial to full separation

Figure 8 has indicated a range of moderate angles of attack (8° to 16° for the current geometry) where leading edge serrations are highly ineffective in reducing aerofoil self-noise. The figure shows that, for the smallest serration wavelength,

noise reductions are negligible while for larger wavelengths, the noise is significantly increased.

Velocity results We first provide an overview of the effect of leading edge serrations on the flow behaviour of the L10H12 serration at the angle of attack of ($\alpha_{eff} \approx 11^\circ$) which has been previously shown in Figure 9b to be ineffective in reducing noise. PIV measurements of the mean and fluctuating components of the streamwise and vertical velocity are made for the baseline aerofoil and for the serrated aerofoil in the planes coinciding with the peak and root. Due to limitations with the PIV setup, measurements were made at the mean flow speed of $U_\infty = 20m/s$, which is half that of the noise measurements. However, we note that these PIV measurements are used only as a means of providing a qualitative understanding of the noise reduction mechanisms.

Figure 16 shows the mean of the streamwise and vertical velocity components for the baseline and serrated aerofoils. Introducing leading edge serrations at this mid-AoA can be seen to have the major effect of shifting the separation further upstream, which is consistent with a shifting of the peak in radiated noise to lower non-dimensional frequencies fc/U , as shown in Figure 9b. Unlike at low AoA, no difference in noise is apparent at frequencies below and above the frequency range where separation noise is dominant.

The RMS values of the fluctuating velocity components are shown in figure 17. The shear layers in each case are clearly defined corresponding to regions of maximum turbulence. The velocity fluctuations are typically 20% greater for the serrated aerofoil compared to the baseline case but are located further from the aerofoil surface. Clearly, therefore, the higher levels of turbulence located further from the aerofoil surface have no appreciable effect on the noise radiation in the frequency range where separation noise is not dominant.

Simultaneous surface pressure and far field noise The previous section has shown that separation occurs further upstream when leading edge serrations are introduced, resulting in the peak radiation occurring at lower frequencies. To quantify the effect of serrations on the causal relationship between pressure fluctuations near the trailing edge and the far field noise, coherence spectra were measured between them using the procedure described in Section above. The coherence spectra were measured for both the baseline aerofoil and the L10H12 serrated aerofoil.

Figure 18 shows the coherence spectra between the pressure measured on the aerofoil suction side closest to the trailing edge (5 mm upstream) and the noise at 1.2 m immediately above the trailing edge at an AoA 11° . Coherence levels of up to 0.5 are observed for the baseline case at $fc/U = 1.5$, indicating a high level of

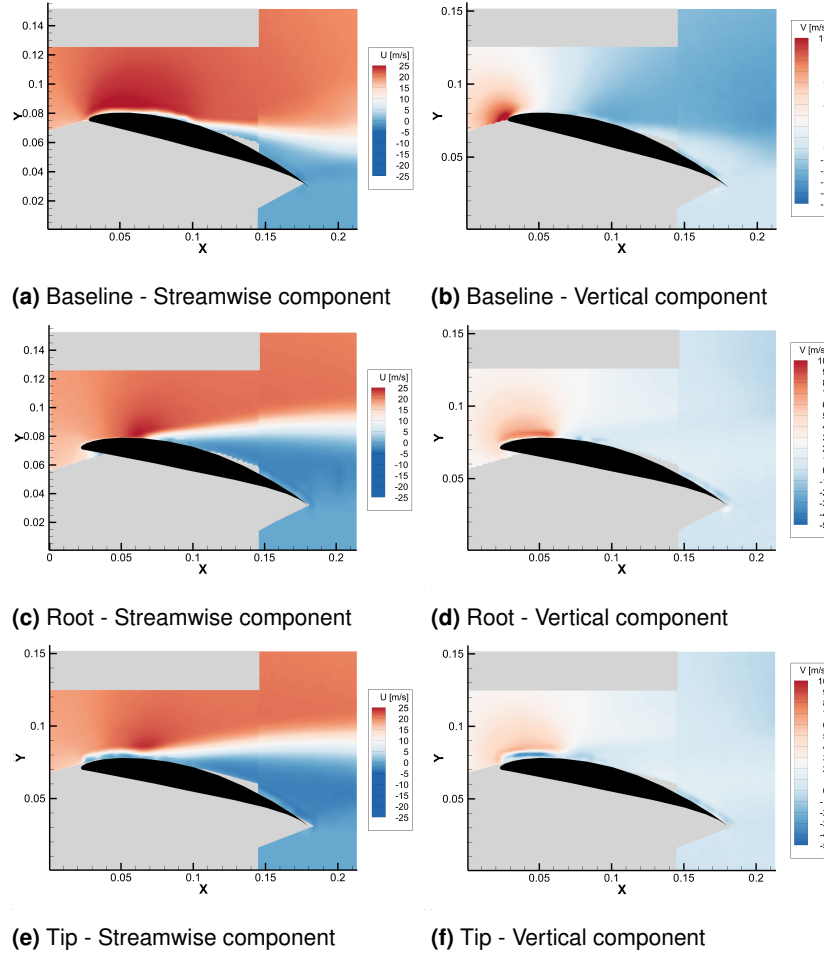


Figure 16. Mean velocity field around the aerofoil for the a), b) Baseline configuration; c), d) Plane crossing the root of the LE serrated configuration; e), f) Plane crossing the tip of the LE serrated configuration.

coherent activity associated with the separated flow. Introducing the serrated leading edge (L10H12) causes a significant reduction in coherence, now peaking at a level of about 0.15 and at a lower frequency of about $fc/U = 0.7$. This shift in frequency is entirely consistent with the shift in the frequency peak associated with separation noise. The coherence between the pressure at a single point within a large separation bubble with the far field radiation is expected to be lower than of a smaller bubble that is more coherent over its spatial extent.

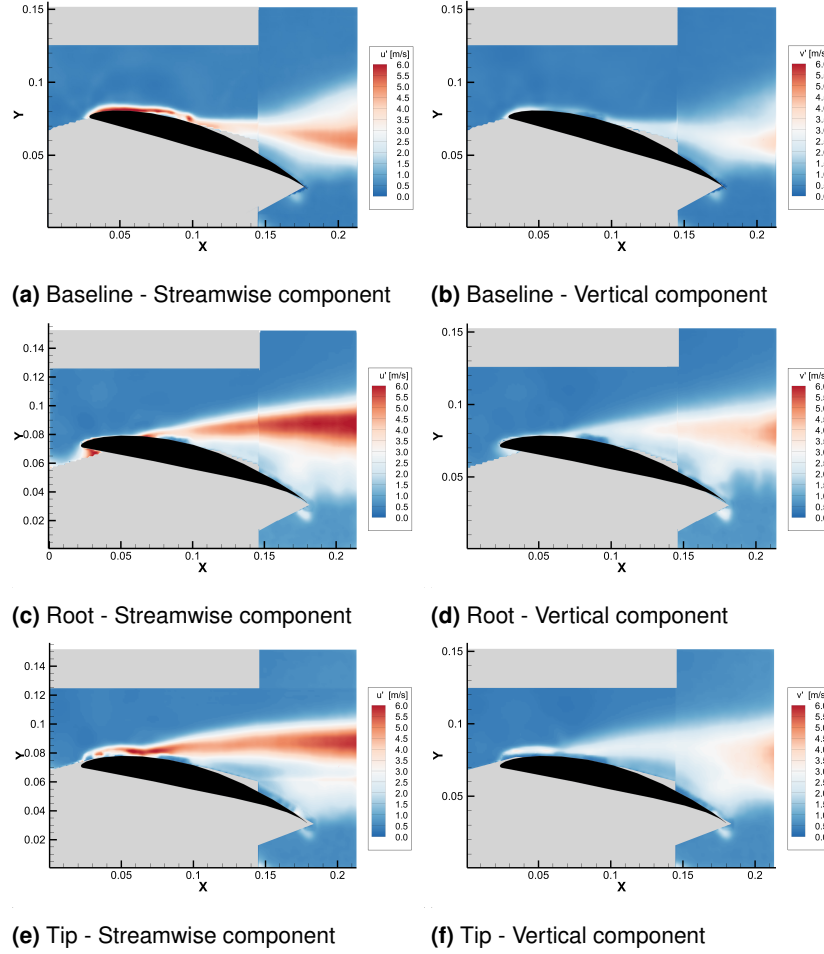


Figure 17. Fluctuating velocity field around the aerofoil for the a), b) Baseline configuration; c),d) Plane crossing the root of the LE serrated configuration; e), f) Plane crossing the tip of the LE serrated configuration.

Simultaneous velocity and unsteady surface pressure measurements We now investigate the coherence between the streamwise velocity fluctuations measured by a single hot wire at various heights above the trailing edge and the surface pressure fluctuations near the trailing edge. The objective of this measurement is to identify the regions in the flow responsible for the surface pressure fluctuations, which in turn radiate to the far field as quantified in the coherence measurements of Figure 18. The measurement was repeated for the baseline and L10H12 serrated aerofoil at the AoA of $\alpha_{eff} = 11^\circ$.

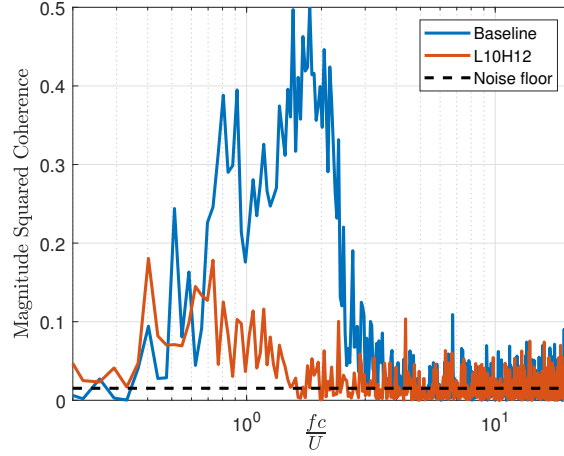


Figure 18. Coherence between noise and surface pressure at TE for baseline and serrated aerofoils at $\alpha_{eff} \approx 11^\circ$

Figure 19 shows colour contours images of the coherence between the measured fluctuating velocity and the surface pressure close to the trailing edge versus non-dimensional frequency St_c and height above the trailing edge. Results are shown for the baseline (left side) and serrated (right side) aerofoils.

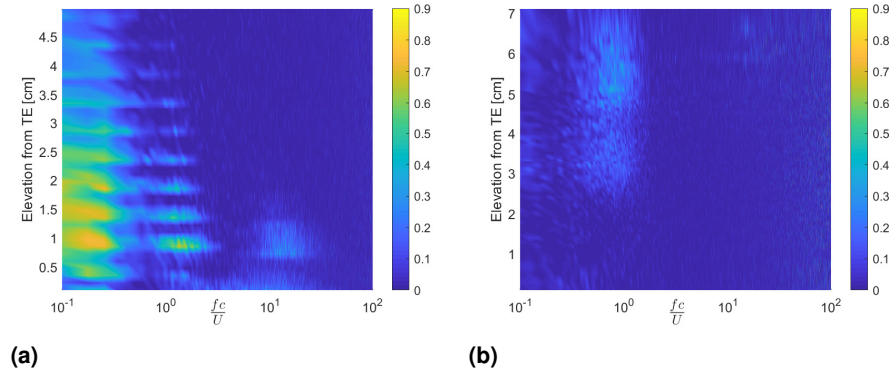


Figure 19. Magnitude squared coherence between velocity and surface pressure at the trailing edge as a function of frequency and spatial location at $\alpha_{eff} \approx 11^\circ$: a) Baseline aerofoil; b) Serrated aerofoil

The coherence contour for the baseline aerofoil can be seen to reveal at least three frequency regions of relatively high coherence (>0.2). The lowest frequency occurs at $St_c \approx 0.15$ and can be associated with a flapping of the shear layer (Zaman et al.

(1987, 1989)) at $St_\alpha = \frac{f c \sin(\alpha)}{U_\infty} \approx 0.03$. The second region corresponds to $St_c \approx 1.5$ and matches the peak frequency in the far field noise spectrum shown in Figure 9b and in the coherence spectrum between the surface pressure and far field noise, as shown in Figure 18. The third, much weaker, source occurs at frequencies of $St_c \approx 15$. The corresponding coherence contour for the serrated aerofoil exhibits only a single source at $St_c \approx 0.7$. This frequency corresponds to the peak frequency in the far field noise spectrum of Figure 9b and also in the coherence spectrum plotted in Figure 19, but has now a relatively weaker coherence level compared to the baseline case. **The reason for this reduced coherence may be due to the larger separation bubble length in streamwise direction compared to the baseline aerofoil. Additionally, the leading edge serrations seems to breaks the spanwise large scale coherence structures resulting in lowered coherence compared to baseline. Note that in both baseline and serrated aerofoil cases the sources appear to be distributed above the shear layer, which is lifted higher in the serrated aerofoil. However, more work is required to prove our hypothesis.**

In summary, therefore, the introduction of leading edge serrations at mid AoA for which the flow is partially to fully separated, has been shown to have a significant effect on the steady and unsteady flow behaviour. The principal effect of the serration is to cause the flow to separate further upstream thereby shifting the peak frequency associated with separation noise to lower frequencies. In the low and high frequency range, for which separation noise is negligible for both the baseline and serrated aerofoils ($fc/U < 0.6$ and $fc/U > 6.0$), the noise radiation is mostly unchanged. When integrated over all frequencies, the overall effect on radiated noise is negligible for the smallest serration wavelength under consideration. The overall effect for the larger wavelength serration is a significant increase in noise.

However, the noise radiation from the baseline aerofoil when the AoA is increased further until the flow has fully separated has been shown in Figure 9c to be significantly reduced by the introduction of leading serration. The reduction mechanism associated with this high AoA regime (regime III) is explored in the next section.

High angles of attack ($AoA \gtrsim 16^\circ$)

Figures 8a and b indicate that leading edge serrations on an aerofoil at high angles of attack, for which the flow has fully separated, are capable of producing overall noise reductions of up to 3 dB. The noise reduction spectra plotted in Figure 9c shows noise reductions over most of the frequency range unlike at low and moderate AoA for which the flow is partially attached.

For completeness the coherence spectrum between the surface pressure close to the trailing edge and the far field microphone for the baseline and L10H12 serrated aerofoil is shown in figure 20 at $\alpha_{eff} = 19^\circ$ where maximum overall noise reductions are obtained. In both cases the coherence is very small (<0.1) over the entire frequency range. This observation is consistent with the conclusion of Paterson et al. (1975) who suggests that for fully stalled aerofoils, noise radiation occurs from the entire chord. The coherence of the far field pressure and a single point on the surface must therefore be negligible.

The absence of any peak in the far field noise spectra plotted in figure 9c and of any peaks in the coherence suggests that noise radiation occurs through the interaction of small-scale turbulence in the shear layer with the aerofoil. This contrasts the radiation mechanism at lower AoA where there is evidence of coherence structures resulting from flow separation.

Two possible mechanisms exist to explain the noise reductions observed at these high AoA. Either the velocity fluctuations in the shear layer have been diminished by the leading edge serrations or the shear layer has been moved further from the aerofoil surface. In the latter case, surface pressure fluctuations will be weaker owing to a larger decay of hydrodynamic pressure from the shear layer to the surface. Unfortunately no velocity data was collected for this high AoA case but it is highly likely that shifting of the shear layer is the dominant noise reduction mechanism, as can be seen in the PIV velocity data at the lower AoA of 11° , where precisely this behaviour can be observed. Finally, we note that at very high AoA of about 22° , no noise reductions can be achieved since both baseline and serrated aerofoils approach the condition similar to a bluff body.

Conclusions

This paper has investigated the performance of leading edge serrations for reducing aerofoil self- noise over a wide range of angles of attack, including pre-stall (flow separated) and post-stall conditions. A comprehensive range of measurements have been realised to quantify the noise reductions for various serration parameters and angles of attack, and also to attempt to understanding the noise reduction mechanism. The study has focused on the NACA65-(12)10 aerofoil, which is amongst a class of high performance aerofoils designed to maximize the region of laminar flow over the surface. While details in the performance may differ for different aerofoils we expect the general behaviour reported here to be broadly valid for a range of different aerofoils.

The main conclusions from this work can be summarized as follows:

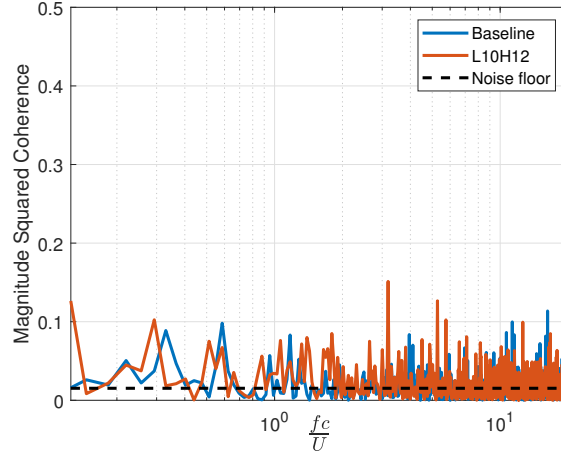


Figure 20. Coherence between noise and surface pressure at the TE for baseline and serrated aerofoils at $\alpha_{eff} \approx 19^\circ$

- The performance of leading edge serration in reducing aerofoil self noise has been shown to fall into three distinct angle of attack regimes, I, II and III.
- Leading edge serrations are able to reduce by up to 3 dB aerofoil self-noise noise at relatively low AoA ($\alpha_{eff} = 4 - 8^\circ$) (regime I), where the flow is mostly attached, and high AoA $\alpha_{eff} > 16^\circ$, where the flow is fully separated (regime III). The noise in the mid range of AoA ($\alpha_{eff} = 8 - 16^\circ$) (regime II) is found to be strongly influenced by the serration wavelength. While smaller wavelength serrations have a negligible effect on noise in this range of angles of attack, larger wavelength serrations are found to cause a significant increase in noise of up to 6 dB.
- For the range of relatively low angles of attack under consideration ($\alpha_{eff} = 4 - 8^\circ$), the serration parameter λ/h has been shown to be important for controlling acoustic performance. Overall self-noise reductions in this range of low AoA are found to improve as λ/h is reduced. In general, noise reductions are obtained for $\lambda/h \lesssim 5$ while small noise increases are obtained above it. The variation in self-noise reductions and aerodynamic performance with λ/h are found to have opposite trends. The optimum serration profile should therefore try to achieve a trade-off between these two considerations.
- The self-noise reduction at relatively low angles of attack can be attributed to a reduction in the boundary layer velocity fluctuations. The modification to the

turbulent boundary layer caused by the leading edge serration has been shown to be consistent with the corresponding reduction in far field noise.

- The poor acoustic performance of leading edge serrations at intermediate angles of attack ($\alpha_{eff} = 8 - 16^\circ$) has been shown to be due to earlier separation on the aerofoil surface causing a shifting of the peak frequency associated with separation noise to lower frequencies with no overall reduction in noise.
- At high angles of attack $\alpha_{eff} > 16^\circ$ self-noise reduction were found to occur over nearly all frequencies which we believe is due to the turbulent shear layer being shifted further from the aerofoil surface by the serration compared to the baseline case. Surface pressure fluctuations on the aerofoil surface are therefore reduced, resulting in a reduction in far field noise.

Acknowledgements

The authors recognize the financial support from the EPSRC Research Grant No: EP/N020413/1 on the “Quiet Aerofoils of the Next Generation” at the University of Southampton.

References

- Fish, F. E., “Influence of hydrodynamic-design and propulsive mode on mammalian swimming energetics,” *Australian Journal of Zoology*, Vol. 42, No. 1, 1994, pp. 79–101.
- Fish, F. E., and Battle, J. M., “Hydrodynamic design of the humpback whale flipper,” *Journal of Morphology*, Vol. 225, No. 1, 1995, pp. 51–60.
- Fish, F. E., Howle, L. E., and Murray, M. M., “Hydrodynamic flow control in marine mammals,” *Integrative and Comparative Biology*, Vol. 48, No. 6, 2008, pp. 788–800.
- Roger, M., Schram, C., and De Santana, L., “Reduction of airfoil turbulence-impingement noise by means of leading-edge serrations and/or porous material,” *19th AIAA/CEAS aeroacoustics conference*, 2013, p. 2108.
- Lau, A. S. H., and Kim, J. W., “The Effects of Wavy Leading Edges on Airfoil-Gust Interaction Noise,” *19th AIAA/CEAS Aeroacoustics Conference*, 2013, p. 2120.
- Clair, V., Polacsek, C., Le Garrec, T., Reboul, G., Gruber, M., and Joseph, P., “Experimental and numerical investigation of turbulence-airfoil noise reduction using wavy edges,” *AIAA journal*, Vol. 51, No. 11, 2013, pp. 2695–2713.
- Chaitanya, P., Joseph, P., Narayanan, S., Vanderwel, C., Turner, J., Kim, J.-W., and Ganapathisubramani, B., “Performance and mechanism of sinusoidal leading edge serrations for the reduction of turbulence–aerofoil interaction noise,” *Journal of Fluid Mechanics*, Vol. 818, 2017, pp. 435–464.

- Hersh, A. S., and Hayden, R. E., "Aerodynamic sound radiation from lifting surfaces with and without leading-edge serrations," *NACA Contr. Rep.*, 1971.
- Gruber, M., Joseph, P., and Chong, T., "On the mechanisms of serrated airfoil trailing edge noise reduction," *17th AIAA/CEAS aeroacoustics conference (32nd AIAA aeroacoustics conference)*, 2011, p. 2781.
- Moreau, D. J., Brooks, L. A., and Doolan, C. J., "Flat plate self-noise reduction at low-to-moderate Reynolds number with trailing edge serrations," *Proceedings of ACOUSTICS*, 2011, pp. 2–4.
- Oerlemans, S., Fisher, M., Maeder, T., and Kögler, K., "Reduction of wind turbine noise using optimized airfoils and trailing-edge serrations," *AIAA journal*, Vol. 47, No. 6, 2009, pp. 1470–1481.
- Geyer, T., Sarraji, E., and Fritzsche, C., "Measurement of the noise generation at the trailing edge of porous airfoils," *Experiments in Fluids*, Vol. 48, No. 2, 2010, pp. 291–308.
- Herr, M., "Design criteria for low-noise trailing-edges," *13th AIAA/CEAS Aeroacoustics Conference (28th AIAA Aeroacoustics Conference)*, 2007, p. 3470.
- Finez, A., Jacob, M., Jondeau, E., and Roger, M., "Broadband noise reduction with trailing edge brushes," *16th AIAA/CEAS Aeroacoustics Conference*, 2010, p. 3980.
- Miklosovic, D., Murray, M., Howle, L., and Fish, F., "Leading-edge tubercles delay stall on humpback whale (*Megaptera novaeangliae*) flippers," *Physics of fluids*, Vol. 16, No. 5, 2004, pp. L39–L42.
- Johari, H., Henoch, C. W., Custodio, D., and Levshin, A., "Effects of leading-edge protuberances on airfoil performance," *AIAA journal*, Vol. 45, No. 11, 2007, pp. 2634–2642.
- Hansen, K. L., Kelso, R. M., and Dally, B. B., "Performance variations of leading-edge tubercles for distinct airfoil profiles," *AIAA journal*, Vol. 49, No. 1, 2011, p. 185.
- Sisinni, G., Pietrogiaconi, D., and Romano, G. P., "Biomimetic wings," *Advances in Science and Technology*, Vol. 84, Trans Tech Publ, 2013, pp. 72–77.
- Hansen, K. L., Rostamzadeh, N., Kelso, R. M., and Dally, B. B., "Evolution of the streamwise vortices generated between leading edge tubercles," *Journal of Fluid Mechanics*, Vol. 788, 2016, pp. 730–766.
- Custodio, D., "The Effect of Humpback Whale-like Protuberances on Hydrofoil Performance," Ph.D. thesis, Worcester Polytechnic Institute, 2007.
- Hansen, K., Kelso, R., and Dally, B., "The effect of leading edge tubercle geometry on the performance of different airfoils," 2009.
- Watts, P., Fish, F. E., et al., "The influence of passive, leading edge tubercles on wing performance," *Proc. Twelfth Intl. Symp. Unmanned Untethered Submers. Technol.*, Auton. Undersea Syst. Inst. Durham New Hampshire, 2001.

- Miklosovic, D. S., Murray, M. M., and Howle, L. E., "Experimental evaluation of sinusoidal leading edges," *Journal of aircraft*, Vol. 44, No. 4, 2007, pp. 1404–1408.
- Skillen, A., Revell, A., Pinelli, A., Piomelli, U., and Favier, J., "Flow over a wing with leading-edge undulations," *Aiaa Journal*, Vol. 53, No. 2, 2014, pp. 464–472.
- Zhang, M., Wang, G., and Xu, J., "Experimental study of flow separation control on a low-Re airfoil using leading-edge protuberance method," *Experiments in fluids*, Vol. 55, No. 4, 2014, p. 1710.
- Van Nierop, E. A., Alben, S., and Brenner, M. P., "How bumps on whale flippers delay stall: an aerodynamic model," *Physical review letters*, Vol. 100, No. 5, 2008, p. 054502.
- Abbott, I. H., and Von Doenhoff, A. E., *Theory of wing sections, including a summary of airfoil data*, Courier Corporation, 1959.
- Chong, T., Joseph, P., and Davies, P., "Design and performance of an open jet wind tunnel for aero-acoustic measurement," *Applied acoustics*, Vol. 70, No. 4, 2009, pp. 605–614.
- Brooks, T., Marcolini, M., and Pope, D., "Airfoil trailing edge flow measurements and comparison with theory, incorporating open wind tunnel corrections," *9th Aeroacoustics Conference*, 1984, p. 2266.
- Willert, C. E., and Gharib, M., "Digital particle image velocimetry," *Experiments in fluids*, Vol. 10, No. 4, 1991, pp. 181–193.
- Raffel, M., Willert, C. E., Kompenhans, J., et al., *Particle image velocimetry: a practical guide*, Springer Science & Business Media, 2007.
- Cierpka, C., Lütke, B., and Kähler, C. J., "Higher order multi-frame particle tracking velocimetry," *Experiments in Fluids*, Vol. 54, No. 5, 2013, p. 1533.
- Soria, J., "An investigation of the near wake of a circular cylinder using a video-based digital cross-correlation particle image velocimetry technique," *Experimental Thermal and Fluid Science*, Vol. 12, No. 2, 1996, pp. 221–233.
- Scarano, F., "Iterative image deformation methods in PIV," *Measurement science and technology*, Vol. 13, No. 1, 2001, p. R1.
- Huang, H., Fiedler, H., and Wang, J., "Limitation and improvement of PIV," *Experiments in fluids*, Vol. 15, No. 4-5, 1993, pp. 263–273.
- Jambunathan, K., Ju, X., Dobbins, B., and Ashforth-Frost, S., "An improved cross correlation technique for particle image velocimetry," *Measurement Science and Technology*, Vol. 6, No. 5, 1995, p. 507.
- Nogueira, J., Lecuona, A., and Rodriguez, P., "Local field correction PIV: on the increase of accuracy of digital PIV systems," *Experiments in fluids*, Vol. 27, No. 2, 1999, pp. 107–116.
- Westerweel, J., and Scarano, F., "Universal outlier detection for PIV data," *Experiments in fluids*, Vol. 39, No. 6, 2005, pp. 1096–1100.

- Anderson Jr, J. D., *Fundamentals of aerodynamics*, McGraw-Hill Education, 2010.
- Brooks, T. F., Pope, D. S., and Marcolini, M. A., "Airfoil self-noise and prediction," *NASA reference publication 1218*, 1989.
- Moreau, S., Roger, M., and Christophe, J., "Flow features and self-noise of airfoils near stall or in stall," *AIAA paper*, Vol. 3198, 2009, p. 2009.
- Schuele, C. Y., and Rossignol, K.-S. S., "Trailing-edge noise modeling and validation for separated flow conditions," *19th AIAA/CEAS Aeroacoustics Conference*, 2013, p. 2008.
- Suryadi, A., and Herr, M., "Wall pressure spectra on a DU96-W-180 profile from low to pre-stall angles of attack," *21st AIAA/CEAS Aeroacoustics Conference*, 2015, p. 2688.
- Bertagnolio, F., Madsen, H. A., Fischer, A., and Bak, C., "A semi-empirical airfoil stall noise model based on surface pressure measurements," *Journal of Sound and Vibration*, Vol. 387, 2017, pp. 127–162.
- Brendel, M., and Mueller, T. J., "Boundary-layer measurements on an airfoil at low Reynolds numbers," *Journal of aircraft*, Vol. 25, No. 7, 1988, pp. 612–617.
- Blake, W. K., *Mechanics of flow-induced sound and vibration, Volume 2: Complex flow-structure interactions*, Academic press, 1986.
- Parchen, R., "A prediction scheme for trailing edge noise based on detailed boundary layer characteristics," *Progress report DRAW*, 1998.
- Amiet, R., "Noise due to turbulent flow past a trailing edge," *Journal of sound and vibration*, Vol. 47, No. 3, 1976, pp. 387–393.
- Kraichnan, R. H., "Pressure fluctuations in turbulent flow over a flat plate," *The Journal of the Acoustical Society of America*, Vol. 28, No. 3, 1956, pp. 378–390.
- Romano, G. P., "Analysis of two-point velocity measurements in near-wall flows," *Experiments in fluids*, Vol. 20, No. 2, 1995, pp. 68–83.
- Stalnov, O., Chaitanya, P., and Joseph, P. F., "Towards a non-empirical trailing edge noise prediction model," *Journal of Sound and Vibration*, Vol. 372, 2016, pp. 50–68.
- Zaman, K., Bar-Sever, A., and Mangalam, S., "Effect of acoustic excitation on the flow over a low-Re airfoil," *Journal of Fluid Mechanics*, Vol. 182, 1987, pp. 127–148.
- Zaman, K., McKinzie, D., and Rumsey, C., "A natural low-frequency oscillation of the flow over an airfoil near stalling conditions," *Journal of Fluid Mechanics*, Vol. 202, 1989, pp. 403–442.
- Paterson, R. W., Amiet, R. K., and Munch, C. L., "Isolated airfoil-tip vortex interaction noise," *Journal of Aircraft*, Vol. 12, No. 1, 1975, pp. 34–40.
- Kim, J.-H., Choi, K.-S., Lacagnina, G., Joseph, P., Hasheminejad, S. M., CHong, T. Z., Shahab, M. F., Omidyeganeh, M., Pinelli, A., "Optimization of leading-edge undulation of a NACA

65(12)-10 aerofoil for noise reduction and aerodynamic enhancement,” *Proceedings of the 23rd International Congress on Acoustics, Aachen, Germany*, 2019.

Lacagnina, G., Chaitanya, P., Berk, T., Kim, J.-H., Joseph, P., Ganapathisubramani, B., Hasheminejad, S. M., CHong, T. Z., Stalnov, O., Choi, K.-S., Shahab, M. F., Omidyeganeh, M., Pinelli, A., “Mechanisms of airfoil noise near stall conditions,” *Physical Review Fluids*, 2019, Vol. 4, 123902.

Narayanan, S., Chaitanya, P., Haeri, S., Joseph, P., Kim, J. W., Polacsek, C., “Airfoil noise reductions through leading edge serrations,” *Physics of Fluids*, Vol. 27, 2015, 025109.